Ohara *et al.*
Progress in Earth and Planetary Science (2023) 10:35
https://doi.org/10.1186/s40645-023-00565-z

Progress in Earth and Planetary Science

RESEARCH ARTICLE

Open Access

Complex evolution of the 2016 Kaikoura earthquake revealed by teleseismic body waves

Kenta Ohara[1], Yuji Yagi[2*], Shinji Yamashita[1], Ryo Okuwaki[2,3], Shiro Hirano[4] and Yukitoshi Fukahata[5]

Abstract

The 2016 Kaikoura earthquake, New Zealand, ruptured more than a dozen faults, making it difficult to prescribe a model fault for analyzing the event by inversion. To model this earthquake from teleseismic records, we used a potency density tensor inversion, which projects multiple fault slips onto a single model fault plane, reducing the non-uniqueness due to the uncertainty in selecting the faults' orientations. The resulting distribution of potency-rate density tensors is consistent with observed surface ruptures. In its initial stage, the rupture propagated northeastward primarily at shallow depths. Later, the rupture propagated northeastward at greater depths beneath a gap in reported surface ruptures. The main rupture phase started in the northeastern part of the Kekerengu fault after 50 s and propagated bilaterally to the northeast and southwest. The non-double-couple component grew to a large fraction of the source elements as the rupture went through the junction of the Jordan Thrust and the Papatea fault, which suggests that the rupture branched into both faults as it back-propagated toward the southwest. The potency density tensor inversion sheds new light on the irregular evolution of this earthquake, which produced a fault rupture pattern of unprecedented complexity. Our source model of the 2016 Kaikoura earthquake (e.g., back-rupture propagation) could prompt research to determine a more realistic model with segmented faults using near-field data.

Keywords Earthquake dynamics, Waveform inversion, Body waves, Earthquake source observation

1 Introduction

On 13 November 2016, the moment magnitude (Mw) 7.8 Kaikoura earthquake struck in the South Island of New Zealand near the boundary between the Pacific and Australia plates (Fig. 1a) (Dziewonski et al. 1981; Ekström et al. 2012). Field studies reported that the earthquake produced a complex set of surface ruptures of more than 12 faults (Hamling et al. 2017; Stirling et al. 2017; Litchfield et al. 2018). The surface rupture area, extending a total length of ∼ 165 km, can be divided into south and north sections separated by a gap of about 30 km with no mapped surface ruptures between the northeast end of the Conway-Charwell fault and the southwest end of the Manakau fault (Litchfield et al. 2018) (Fig. 1b). The south section involved the Humps fault and the Conway-Charwell fault with mixed dextral and reverse faulting (Litchfield et al. 2018) (Fig. 1b). The north section displayed a linear set of surface ruptures with mixed vertical and dextral displacements on the Manakau fault, the Upper Kowhai fault, the Jordan Thrust, the Kekerengu fault, and the Needles fault (Litchfield et al. 2018). In addition, surface rupture with mixed sinistral and reverse offsets occurred on the west-dipping Papatea fault, which extends southward nearly orthogonal to the linear rupture set near the junction of the Kekerengu fault

*Correspondence:
Yuji Yagi
yagi-y@geol.tsukuba.ac.jp
[1] Graduate School of Science and Technology, University of Tsukuba, Tsukuba, Ibaraki 305-8572, Japan
[2] Faculty of Life and Environmental Sciences, University of Tsukuba, Tsukuba, Ibaraki 305-8572, Japan
[3] Mountain Science Center, University of Tsukuba, Tsukuba, Ibaraki 305-8572, Japan
[4] College of Science and Engineering, Ritsumeikan University, Kusatsu, Shiga 525-8577, Japan
[5] Disaster Prevention Research Institute, Kyoto University, Uji, Kyoto 611-0011, Japan

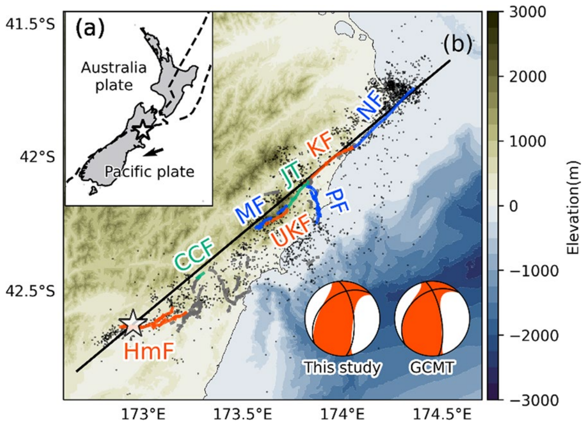

Fig. 1 **a** Tectonic setting of the study region. The dashed lines represent the plate boundary (Bird 2003). The arrow denotes the plate motion of the Pacific plate relative to the fixed Australia plate in NUVEL 1A (DeMets et al. 1994). The star marks the mainshock epicenter (Lanza et al. 2019). **b** Seismotectonic summary of the study region of the 2016 Kaikoura earthquake. The left and right beach ball shows the obtained total moment tensor and the Global Centroid Moment Tensor (Dziewonski et al. 1981; Ekström et al. 2012) for the mainshock, respectively. Black dots represent aftershocks during the week after the mainshock (Lanza et al. 2019). Gray, orange, blue, and green lines indicate surface ruptures of the 2016 Kaikoura earthquake from the New Zealand Active Faults Database (Langridge et al. 2016). The black line represents the assumed model plane. Background contours display topography/bathymetry (Mitchell et al. 2012). HmF–Humps fault zone, CCF–Conway-Charwell fault, MF–Manakau fault, UKF–Upper Kowhai fault, JT–Jordan Thrust, PF–Papatea fault, KF–Kekerengu fault, NF–Needles fault

and the Jordan Thrust (Litchfield et al. 2018) (Fig. 1b). Aftershocks were distributed throughout the zone of surface ruptures (Lanza et al. 2019) (Fig. 1b).

The Global Centroid Moment Tensor (GCMT) solution for the mainshock (Dziewonski et al. 1981; Ekström et al. 2012) indicates oblique reverse faulting (Fig. 1). A multiple-point-source inversion using the records of long-range seismographs (teleseismic waveforms) detects four subevents, consisting of three oblique strike-slip subevents and one thrust subevent (Duputel and Rivera 2017), indicating that the earthquake ruptured multiple faults with different faulting mechanisms. Finite-fault inversions using seismic data alone (Bai et al. 2017; Hollingsworth et al. 2017; Zhang et al. 2017; Zheng et al. 2018) or using both seismic and geodetic data (Cesca et al. 2017; Holden et al. 2017; Wang et al. 2018b) commonly find the initial rupture episode during the first ~60 s, followed by the main rupture episode, and discuss the rupture propagated toward northeast from the epicenter in both episodes. Notably, the field surveys identify large displacements with sinistral and reverse offsets at the Papatea fault (Clark et al. 2017; Hamling et al. 2017; Stirling et al. 2017; Litchfield et al. 2018).

However, finite-fault inversions using only teleseismic body waves, which can estimate the overall rupture propagation process during an earthquake, have not identified subevents with focal mechanism corresponding to that Papatea fault rupture (Bai et al. 2017; Hollingsworth et al. 2017; Zhang et al. 2017).

Finite-fault inversions in previous studies estimated the rupture process under the assumption that the rupture unilaterally propagates northeastward (Bai et al. 2017; Cesca et al. 2017; Holden et al. 2017; Hollingsworth et al. 2017; Zhang et al. 2017; Wang et al. 2018b; Zheng et al. 2018). Such small constraints on the unilateral rupture scenario may not always be appropriate for the earthquake modeling in a complex fault zone, which sometimes involves irregularity, e.g., the rupture in the backward direction as a part of its bilateral propagation that is initiated as a secondary rupture episode (e.g., Gallovič et al. 2020; Yamashita et al. 2022a; Yagi et al. 2023). The assumption of unilateral northeastward rupture propagation can make the interpretation of the inversion results more difficult. Indeed, it is difficult to explain how a right-lateral strike-slip rupture propagating in a northeast direction along the Jordan Thrust could have triggered a reverse fault rupture on the Papatea fault, situated in the extensional quadrant of the focal mechanism of the Jordan Thrust. Therefore, there should still be a room to investigate whether alternatives to the unilateral rupture scenario proposed by finite-fault inversions exist.

As the 2016 Kaikoura earthquake includes multiple faults and complex fault geometries, finite-fault inversion assuming one or a few simplified model fault planes may produce erroneous inversion results due to modeling errors caused by the inappropriate assumed fault geometries (Shimizu et al. 2020). This motivates using a potency density tensor inversion (PDTI) (Shimizu et al. 2020), that is not requiring assumption of fault geometries, to estimate the rupture process of the 2016 Kaikoura earthquake along an assumed model plane. The PDTI incorporates the uncertainty of the Green's function in the data covariance matrix (Yagi and Fukahata 2011) and introduces the Akaike's Bayesian information criterion (ABIC) (e.g., Akaike 1980, Yabuki and Matsu'ura 1992, Sato et al. 2022), making it possible to perform stable inversion using seismic source model with a high degree of freedom in the rupture direction (e.g., Hicks et al. 2020; Yamashita et al. 2022a; Yagi et al. 2023).

In this study, we applied the PDTI to teleseismic P-waveforms of the 2016 Kaikoura earthquake to simultaneously estimate the rupture propagation and the focal mechanism variation. It revealed a source process consisting of an initial and a main rupture episode. The initial rupture propagates northeast from the hypocenter and breaks shallow and deep parts of the source area; deep rupture occurs where there is no surface rupture reported. Then, the main rupture begins at the northeast end of the Kekerengu fault and propagates bilaterally to the northeast and southwest. The southwestward rupture (backward rupture) branches out and propagates into the Jordan Thrust and the Papatea fault.

2 Methods, data, and modeling

The PDTI of teleseismic P-waveforms has been developed to mitigate the effect of modeling errors due to an inaccurate model fault geometries (Shimizu et al. 2020). Teleseismic P-waveforms are sensitive to perturbations in the focal mechanism but insensitive to errors in the source location, which is confirmed by both the synthetic tests and real applications (e.g., Shimizu et al. 2020; Tadapansawut et al. 2022; Yamashita et al. 2022b). Therefore, it is important to incorporate the focal mechanism change during the rupture propagation when building a seismic source model to robustly estimate the rupture process (Shimizu et al. 2020). Whereas the conventional finite-fault inversion method estimates the slip distribution along the fault plane as a potency density distribution, the PDTI method adopted in this study describes the fault slip along the assumed model plane as a superposition of five basis double-couple (Kikuchi and Kanamori 1991) and then estimates the rupture evolution (including perturbations in the focal mechanism) as a spatiotemporal distribution of the potency-rate density tensor. Thus, the seismic waveform u_j observed at a station j is given by

$$u_j(t) = \sum_{q=1}^{5} \int_S \left(G_{qj}(t,\xi) + \delta G_{qj}(t,\xi) \right) * \dot{D}_q(t,\xi) d\xi + e_{bj}(t),$$

where G_{qj} is the Green's function of the qth basis double-couple moment tensor, δG_{qj} is the modeling error on G_{qj} (Yagi and Fukahata 2011), $\dot{D}_q$ is the potency-rate density function for the qth component of the basis double-couple moment tensor, e_{bj} is a background and instrumental Gaussian noise, ξ represents a position on the assumed model plane (S), and $*$ denotes the convolution operator in the time domain. Following Yagi and Fukahata (2011), the background noise level is assessed by referring to the pre-signal data, and the variance of the Green's function error is set to be proportional to the amplitude of the Green's function.

Because this inversion allows any type of a deviatoric focal mechanism on the assumed model plane, information about the fault geometry can be extracted from the observed data (Shimizu et al. 2020). To stably invert such a high degree-of-freedom seismic source model, the PDTI introduces the error term of the Green's function into the data covariance matrix (Yagi and Fukahata 2011) and then evaluates the relative weights of information from observed data and prior constraints using Akaike's Bayesian information criterion (ABIC) (Akaike 1980, Yabuki and Matsu'ura 1992, Sato et al. 2022). This inversion formulation reduces the effect of modeling errors caused by uncertainties in fault geometry and Green's function and allows stable estimates of the seismic source process even when the predefined model plane deviates from the true fault plane (Shimizu et al. 2020). The PDTI has been effectively applied to earthquakes for which it is difficult to assume a reasonable fault model (Okuwaki et al. 2020, 2021; Tadapansawut et al. 2021; Yamashita et al. 2021, 2022a; Okuwaki and Fan 2022). The PDTI is thus suitable for analyzing the 2016 Kaikoura earthquake.

The data covariance matrix, which introduces the error term of the data covariance matrix, is a function of the model parameter (Yagi and Fukahata 2011). This means that the inverse problem to be solved in PDTI becomes nonlinear. Following Yagi and Fukahata (2011), we set initial model parameters and solve the nonlinear problem iteratively by improving the model parameters (Shimizu et al. 2020).

For the PDTI, we used the teleseismic P-waveforms (vertical component) from 48 stations at epicentral distances of 30°–100° downloaded from the Data Management Center of the Incorporated Research Institutions for Seismology (IRIS-DMC) (Fig. 2a). We converted the raw waveform data to velocity waveforms at a sampling interval of 0.8 s. We calculated Green's functions at a sampling interval of 0.1 s by the method of Kikuchi and Kanamori (Kikuchi and Kanamori 1991). We used CRUST2.0 (Bassin et al. 2000) as a 1-D structure model around the source (see Additional file 1: Table S1) and set the value of t^*, which controls the inelastic attenuation of P-waves, to 1 s. The ray parameters and geometrical spreading factors were calculated based on the ak135 reference velocity model (Kennett et al. 1995). We manually picked and aligned the P-wave first motion to correct the travel-time deviations due to 3-D earth structure (e.g., Fan and Shearer 2015). The effect of uncertainty of underground structure was mitigated by introducing the error term of the Green's function into the data covariance matrix (Yagi and Fukahata 2011).

Because the high-frequency component of the teleseismic body waveforms is effectively suppressed owing to the natural low-pass filtering caused by inelastic attenuation, given resampling interval of 0.8 s, the waveforms are only little affected by aliasing (see Additional file 1: Fig. S1). Conversely, applying a low-pass filter that includes an anti-aliasing filter increases the off-diagonal component of the data covariance matrix (Yagi and Fukahata

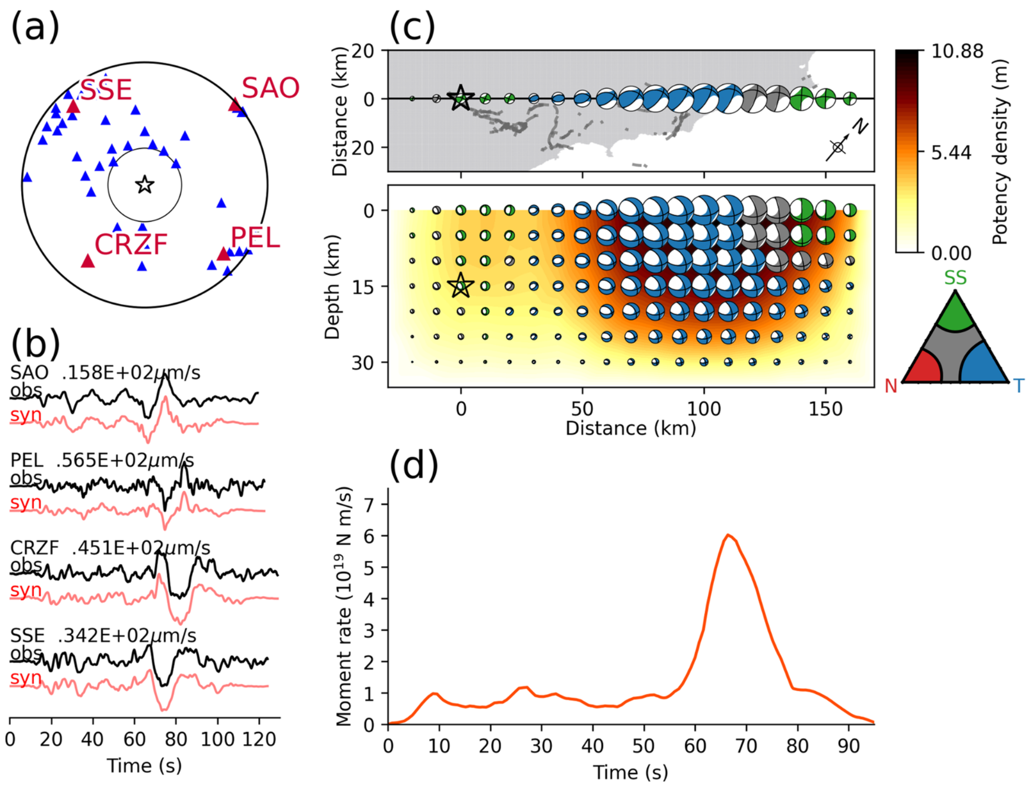

Fig. 2 Summary of inversion results. **a** Azimuthal equidistant projection of the station distribution used in the inversion. The star denotes the epicenter (Lanza et al. 2019). Triangles denote station locations; the waveforms for the four stations indicated with red triangles are shown in **b**. The circles represent epicentral distances of 30° and 100°. **b** Observed (upper black trace) and synthetic (lower red trace) waveforms at the stations marked in red in **a**. Station codes and maximum amplitudes are shown at the top. **c** Potency density tensors on the assumed model plane. The map view in the top panel shows the top row of tensors on the assumed model plane, represented by the black line, and gray lines indicate surface ruptures (Langridge et al. 2016). The profile in the bottom panel shows the tensors on the assumed model plane. Note that the beach balls in the map are shown as a lower-hemisphere projection in the map and as a cross-section view from the southeast side in the bottom panel. Beach balls in the bottom panel are colored based on a Frohlich diagram (Frohlich 2001), in which blue is reverse faulting (T), green is strike-slip faulting (SS), red is normal faulting (N), and gray is other. The star denotes the hypocenter (Lanza et al. 2019). **d** Moment-rate function

2011), making it difficult to stably invert the data covariance matrix. Therefore, we do not make any low-pass filtering of real and synthetic data and are able to reproduce observed waveforms well (Fig. 2b, Additional file 1: Fig. S2).

We adopted a hypocenter location at 172.95° E, 42.62° S, and 15 km depth (Lanza et al. 2019). We established a 200 km × 35 km vertical model plane striking NE–SW (230°) to represent surface ruptures (Langridge et al. 2016; Hamling et al. 2017; Stirling et al. 2017; Litchfield et al. 2018) and aftershock activity (Lanza et al. 2019) (Fig. 1b). We set a maximum rupture velocity of 2.6 km/s to allow for the northeastward migration of the high-frequency source at about 2.0 km/s indicated by P-waveform back-projection (Xu et al. 2018). The slip on the model plane was expanded by linear B-spline functions in space with an interval of 10 km and 5 km in the strike and dip directions, respectively, and by linear B-spline functions in time with an interval of 0.8 s with a maximum duration of 60 s for each source element, which is long enough to detect possible re-rupture and/or back-rupture propagation (Holden et al. 2017; Hicks et al. 2020). The total duration of the event was set to 95 s. The ABIC can prevent overfitting, even using large number of model parameters (Sato et al. 2022).

We applied a time-adaptive smoothing constraint that adjusts the smoothing strength in inverse proportion to the changing amplitude of the potency-rate function (Yamashita et al. 2022b). This constraint can mitigate the problem of oversmoothing during the main rupture, which obscures the results (Yamashita et al. 2022b).

3 Results

We estimated the distribution of potency-rate density tensors on the assumed vertical model plane and then time-integrated them at each source element to yield the spatial distribution of potency density tensors shown in Fig. 2c. This figure shows an area of high potency density centered around 110 km northeast of the epicenter on the shallow part of the model plane. The dominant focal mechanism (with relatively large potency density) differs along the length of the fault plane, being oblique reverse slip for 50–120 km and strike-slip for 130–150 km northeast of the epicenter (Fig. 2c). The total seismic moment is 1.1×10^{21} Nm (Mw 8.0). The moment-rate function of the whole source process, obtained by calculating the seismic moment rate of the best-fitted double-couple source at each sampling time, is around 1.0×10^{19} Nm/s until 55 s from the origin time and then increases rapidly, reaching 6.0×10^{19} Nm/s at 66 s (Fig. 2d).

Figure 3 shows selected snapshots of the potency-rate density tensors on a cross section of the model fault plane; see Additional file 1: Fig. S3 for the full set of snapshots. Figure 4 shows a map view of the strike angles of the nodal planes of these tensors along the top of the model plane. During the first 10 s from the origin time, a strike-slip rupture striking about 25° clockwise from the

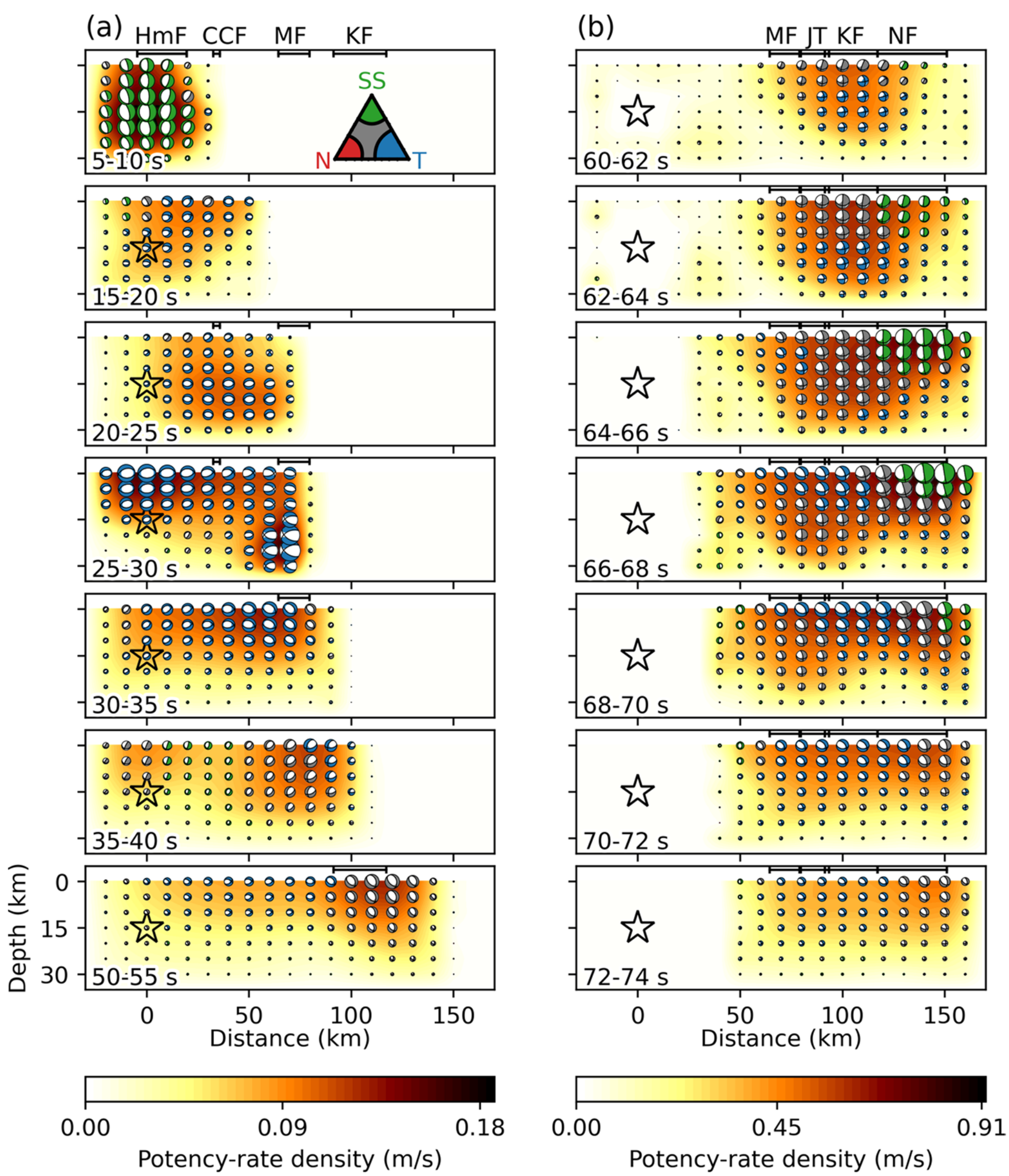

Fig. 3 Selected snapshots of potency-rate density tensors **a** before 55 s and **b** after 60 s. Beach balls are shown in cross-section view from the southeast side of the assumed model plane. The background color is scaled with the maximum potency-rate density during 0–55 s for (**a**) and 60–74 s for (**b**); note that the scales differ for the two plots. The star denotes the hypocenter (Lanza et al. 2019). Black bars are the locations of the surface faults (Langridge et al. 2016) projected onto the model plane

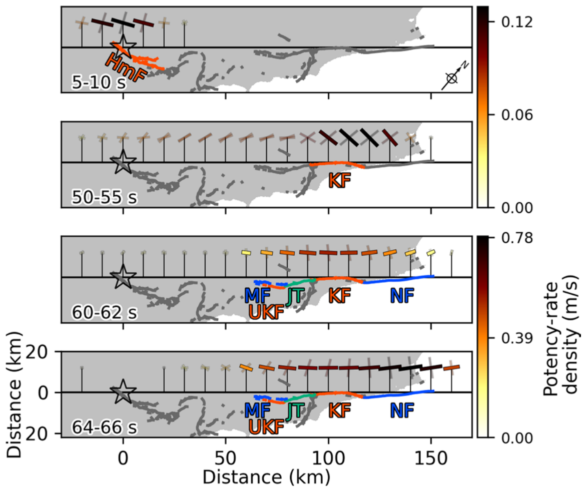

Fig. 4 Map views showing selected snapshots of strikes of the potency-rate density tensors (cross-marks) in the top row of the model plane. Right-lateral or northwest-dipping nodal planes of tensors with relatively large potency-rate density are emphasized. Note that the color scale changes after 55 s

model plane propagated to the northeast of the epicenter (Figs. 3a and 4). Hereafter, we refer to the origin time as 0 s. The rupture then propagated further northeastward on the shallow part of the model plane, changing to an oblique reverse focal mechanism. This shallow rupture stagnated at about 40 km northeast of the epicenter after 20 s; however, a deeper rupture continued on the model plane between 20 and 30 s, reaching 70 km northeast of the epicenter. An isolated reverse rupture occurred at 25–30 s near the ground surface around the epicenter. During 30–45 s, an oblique reverse rupture appeared near the ground surface about 70 km northeast of the epicenter and propagated northeast; between 45 and 50 s, the rupture propagation pattern was obscure (see Additional file 1: Fig. S3a).

After 50 s, the main rupture emerged near the ground surface about 110 km northeast of the epicenter and propagated bilaterally to the northeast and southwest (Fig. 3 and Additional file 1: Fig. S4). Between 50 and 55 s, the dominant focal mechanisms were mixed reverse and strike-slip with the right-lateral nodal plane oriented about 40° clockwise from the model plane (Figs. 3a and 4). The northeastward rupture, a strike-slip rupture striking about 10° counterclockwise from the model plane, propagated through the shallow part of the model plane and reached the edge of the model plane at about 68 s (Figs. 3b and 4). The southwestward rupture reached about 70 km northeast of the epicenter by 70 s (Fig. 3b). Between 60 and 64 s, it was dominantly strike-slip near the ground surface and reverse in the deep part of the model plane (Fig. 3b). The reverse slip component increased with time after 64 s. The rupture gradually weakened after 70 s and ceased at 95 s. The inverted solution well explains the teleseismic P-waveforms (Fig. 2b, Additional file 1: Fig. S2).

4 Reproducibility and sensitivity tests

We performed a numerical experiment to test the stability and reproducibility of our potency-rate density tensor distribution. We used the obtained source model as an input model and generated input synthetic waveforms for the 48 stations used in the analysis. As an error of Green's function, we assumed random Gaussian noise with zero mean and a standard deviation of 3% of maximum amplitude of each calculated Green's function. As the background noise, we assumed random Gaussian noise with zero mean and a standard deviation of 1 μm. The input synthetic waveform was produced by adding background noise to the convolved Green's function with error and the input slip-rate function (see Additional file 1: Fig. S5). The input synthetic waveforms were inverted with the same settings used with the real waveforms.

We performed a structure sensitivity test using the 1-D structure model CRUST1.0 (Laske et al. 2013) for the source region instead of CRUST2.0 (Bassin et al. 2000) (see Additional file 1: Table S2). We estimated the rupture evolution using the same observed dataset and the same inversion settings as for our preferred modeling.

We also performed another sensitivity test projecting rupture process onto a horizontal model plane. We established a 200 km × 70 km horizontal model plane striking NE–SW (230°) to represent surface ruptures (Langridge et al. 2016; Hamling et al. 2017; Stirling et al. 2017; Litchfield et al. 2018) and aftershock activity (Lanza et al. 2019) (see Additional file 1: Figs. S8 and S9). The slip on the model plane was expanded by bilinear B-spline functions in space with an interval of 10 km. The hypocentral depth was 10 km, where rupture mainly detected in the analysis using vertical model plane (Figs. 2 and 3). We used the same observed dataset and the same inversion settings as for our preferred modeling using the vertical plane.

Both the reproducibility and structure sensitivity tests successfully reproduced the robust features in our preferred model: These included the initial strike-slip rupture during the first 10 s, the northeast-propagating oblique reverse rupture at varying depths between 10 and 30 s and re-appearing near the ground surface about 70 km northeast of the epicenter, and the main bilateral rupture starting about 110 km northeast of the epicenter around 50 s with a strike-slip rupture propagating northeast and an oblique-slip rupture propagating southwest (see Additional file 1: Figs. S6, S7, and S8). In the reproducibility test, however, potency-rate density tensors between 25 and 35 s at 50–100 km northeast of the epicenter show reverse faulting in the input model but strike-slip in the output model, and potency-rate density distribution between 40 and 50 s is different between the input and output models (Additional file 1: Fig. S6). As these features are not robustly reproduced in this exercise, we do not discuss them in the following section.

The sensitivity test using the horizontal model plane reproduced the lateral variation of rupture evolution in the preferred source model using the vertical model plane: the initial strike-slip rupture during the first 10 s, the northeast-propagating oblique reverse rupture between 10 and 30 s, and the main bilateral rupture from about 110 km northeast of the epicenter (see Additional file 1: Figs. S9 and S10). However, the sensitivity test shows different potency-rate density tensors from those in the preferred source model: Potency-rate density tensors between 25 and 30 s at about 70 km northeast of the epicenter had P-axes rotated counterclockwise by about 90° from those in the preferred source model, and potency-rate density tensors between 60 and 66 s at 70–120 km northeast of the epicenter show reverse faulting in the sensitivity test, whereas those in the preferred source model show strike-slip and oblique slip. In general, the teleseismic waveforms contain depth phases, but the horizontal model plane cannot reproduce these variations, which may have contributed to the discrepancy between the vertical and horizontal model planes (Shimizu et al. 2020; Yamashita et al. 2022b).

5 Discussion

Our result shows that the rupture process of the 2016 Kaikoura earthquake can be divided into initial and main rupture episodes: the initial rupture propagated northeastward; the main rupture propagated bilaterally from 110 km northeast of the epicenter, involving backward rupture propagation toward the epicenter. The total moment tensor, which is obtained by integrating the potency-rate density tensors in space and time, shows oblique reverse faulting, which is consistent with the GCMT solution (Fig. 1). Our estimated total seismic moment is 1.1×10^{21} Nm (Mw 8.0), which is larger than the GCMT solution (6.7×10^{20} Nm; Mw 7.8). The discrepancy between our estimates of the seismic moment and those from the other inversion methods may be due to a simplified seismic source model that may not be adequate to represent the complex source process. In the following, we will discuss how those rupture episodes relate to the observed surface ruptures, to unravel the unprecedentedly complex rupture process of the 2016 Kaikoura earthquake.

As the initial strike-slip rupture propagated northeast during the first 10 s (Fig. 3a), the right-lateral nodal planes of the potency-rate density tensors matched the strike of the Humps fault (Langridge et al. 2016) (Fig. 4). Hereafter, we interpret right-lateral or northwest-dipping nodal planes as fault planes, because right-lateral strike-slip or northwest-directing dip slip is dominant in surface faults reported in field surveys (Clark et al. 2017; Hamling et al. 2017; Stirling et al. 2017; Litchfield et al. 2018). An oblique reverse rupture then propagated northeast through the shallow part of the model plane. After 20 s, the shallow rupture stagnated about 40 km northeast of the epicenter, while the oblique reverse rupture continued to propagate deeper on the model plane (Fig. 3a). The location where the shallow rupture stagnated corresponds to the gap in surface ruptures between the Conway-Charwell and Manakau faults (Langridge et al. 2016) (Figs. 1 and 3a), and the deep oblique reverse slip has also been identified by the finite-fault inversion of geodetic data (Hamling et al. 2017). Between 30 and 35 s, oblique reverse rupture appeared near the ground surface about 70 km northeast of the epicenter, corresponding to the southwest end of the Manakau fault (Langridge et al. 2016), and then propagated near the ground surface until 45 s (Fig. 3a). Our results show that the initial rupture shifted deeper around the area of no surface rupture between 20 and 30 s. However, because slips on multiple fault planes are projected onto the single model plane in our inversion, it is difficult to determine whether these ruptures were connected at depth.

It is controversial how the plate interface contributed to moment release in the 2016 Kaikoura earthquake (e.g., Lanza et al. 2019). Although the deep rupture between 20 and 30 s appeared at about 25 km depth, the resolved dip angles (~40°) are steeper than those of the hypothesized plate interface (e.g., Williams et al. 2013). Our solution is still limited to be conclusive about a cause of the rupture at depth to reach Kekerengu fault. This may be realized by a listric geometry of faults connecting at depth (e.g., Xu et al. 2018), or the Kekerengu fault could be connected at depth via the Point Keen fault (e.g., Ulrich et al. 2019). We note here that our bilateral rupture scenario would be useful to further constrain the rupture dynamics of the relevant deep faults by the independent studies such as physics-based rupture simulation.

After 50 s, the main rupture appeared in the northeast part of the Kekerengu fault (Langridge et al. 2016) and then propagated bilaterally until about 70 s, such that one end of the rupture appeared to propagate backward toward the epicenter (Fig. 3). Because we cannot trace the rupture migration between 45 and 50 s, it is difficult to determine how the initial rupture migrated to the main rupture. The potency-rate density tensors obtained at 50–55 s indicate both strike-slip and reverse faulting, and the strikes of their right-lateral nodal planes are consistent with that of the northeastern Kekerengu fault (Langridge et al. 2016) (Fig. 4). For the northeastward strike-slip rupture, the strikes of the right-lateral nodal planes match the orientation of the Needles fault (Langridge et al. 2016) (Fig. 4), and the dominance of strike-slip faulting in the shallow part of the model plane (Fig. 3b) is consistent with other studies (Bai et al. 2017; Cesca et al. 2017; Hollingsworth et al. 2017; Wang et al. 2018a, 2018b; Zheng et al. 2018; Xu et al. 2018; Mouslopoulou et al. 2019). For the backward rupture, the potency-rate density tensors near the ground surface show a transition from oblique strike-slip to oblique reverse faulting 80–110 km northeast of the epicenter (Fig. 3b), and the strikes of the right-lateral or northwest-dipping nodal planes match those of the central Kekerengu fault and the Jordan Thrust (Langridge et al. 2016) (Fig. 4).

The potency-rate density tensors around the Jordan Thrust and Papatea fault contain large non-double-couple components, reaching an 80% maximum from 60 to 66 s, that then rapidly decrease to less than 20% after 66 s (Fig. 5). Our reproducibility tests also captured the time variation of this component (see Additional file 1: Figs. S6 and S7). The size of the non-double-couple component from 60 to 66 s suggests that large non-double-couple component is just apparent, and real rupture might have been 100% double-couple but slips occurred on multiple faults with different orientations (e.g., Liu and Zahradník 2020; Turhan et al. 2023); this is consistent with reverse faulting with sinistral strike-slip reported on the Papatea fault (Hamling et al. 2017; Stirling et al. 2017; Litchfield et al. 2018; Wang et al. 2018b; Xu et al. 2018), which is nearly perpendicular to the other surface ruptures (see Additional file 1: Fig. S11). Our result suggests that the backward rupture on the Kekerengu fault not only propagated into the Jordan Thrust, but also branched out and propagated into the Papatea fault. Given that the right-lateral strike-slip rupture propagates in a southwest direction along the Kekerengu fault, the Papatea fault is situated in the compressional quadrant; this suggests that the southwestward rupture along the Kekerengu fault can better explain a trigger of the reverse faulting rupture along the Papatea fault than the northeastward rupture along the Jordan Thrust, which should require the Papatea fault to be located in the extensional quadrant. Although we find it reasonable to explain the Papatea rupture by our series of bilateral ruptures, more detailed analyses and simulations incorporating the detailed geometries of those faults will be required to testify which of the scenarios is more favorable for the Papatea rupture. Near the southwest end of the backward rupture of the Jordan Thrust and Papatea fault, the strikes of the right-lateral or northwest-dipping nodal planes were about 10° clockwise from the model plane, which is consistent with the strikes of the Upper Kowhai and Manakau faults (Langridge et al. 2016) (Fig. 4).

The Papatea Fault has been a key element and its role in rupture propagation and deformation have been actively discussed (e.g., Kilinger et al. 2018; Ulrich et al. 2019). In particular, the seismological findings seem to have apparently diverging view of the rupture timing of the Papatea faulting (e.g., Xu et al. 2018; Wang et al. 2018a, b). Our study here is proposing that, based on our estimates of rupture timing and the fault geometry, the rupture proceeds from the Kekerengu to Papatea faults as a part of the bilateral rupture propagation.

So far, an earthquake source modeling has often been relying on a restricted degree of freedom, which has been considered as a requirement for a plausible solution. However, the modeling employing fewer degrees

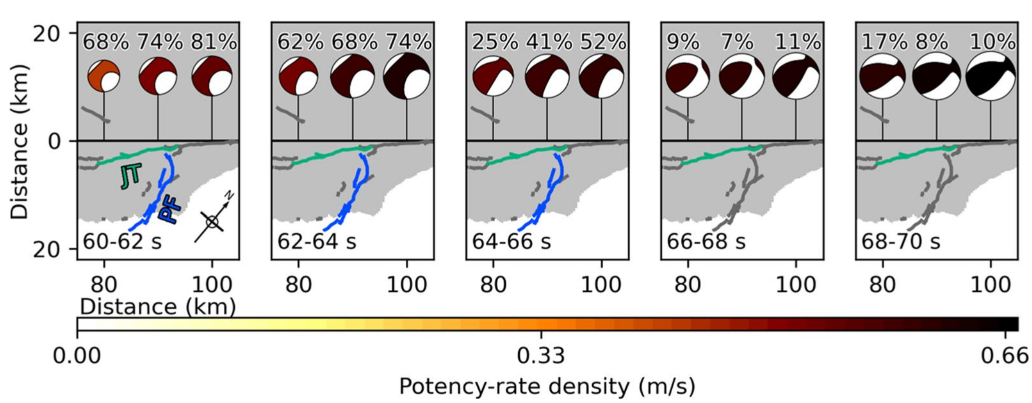

Fig. 5 Map views showing selected snapshots of potency-rate density tensors (lower-hemisphere projections) between 60 and 70 s in the top row of the model plane 80–100 km northeast of the epicenter. The color of the beach ball symbols represents the potency-rate density. Above each symbol is shown the ratio of the apparent non-double-couple component that arises from mixing faulting types

of freedom might be easy to drop information that are recorded in the observed data and critical to interpret the source process (e.g., Shimizu et al. 2020), albeit the solution derived from those modeling apparently looks not bad. One of the advantages of employing a model with a high degree of freedom (e.g., this study) is that a solution is less susceptible to the modelers' preconceptions. By estimating the potency tensor density distribution including the non-double-couple component, we found that the backward rupture branched out and propagated on the Papatea fault, which, to our best knowledge, has not been reported in previous attempts of the teleseismic body waves analyses.

Our analysis suggests the following scenario for the main rupture: It propagated bilaterally from the northeast part of the Kekerengu fault, the northeastward rupture propagating along the Needles fault and the southwestward rupture propagating along the Kekerengu fault, Jordan Thrust, Papatea, Upper Kowhai, and Manakau faults. We interpret the simultaneous rupture events in the area around the Needles fault and the Jordan Thrust noted in previous studies (Bai et al. 2017; Cesca et al. 2017; Hollingsworth et al. 2017) as bilateral rupture propagation. In addition, the back-projection image (Xu et al. 2018) shows that the seismic wave radiation point moves toward the epicenter from around the south edge of the Papatea fault between 50 and 70 s, a finding consistent with backward rupture propagation.

In the region of the backward rupture, multiple faults may have ruptured during the initial rupture phase, because the aftershock region extends perpendicular to the model plane and the focal mechanisms varied during the initial rupture (Fig. 6). Because our model fault plane may include projections of multiple independent ruptures, we cannot determine which faults participated in the initial rupture. Therefore, we cannot say whether the backward rupture was a re-rupture (Holden et al. 2017) or a rupture on a different fault, as in the 2010 El Mayor–Cucapah earthquake (Yamashita et al. 2022a).

Back-propagating ruptures in seismic events are not so rare; they have been reported in the 2010 El Mayor–Cucapah earthquake (Yamashita et al. 2022a), the 2011 Tohoku-Oki earthquake (Ide et al. 2011), the 2014 Iquique earthquake (Yagi et al. 2014), the 2016 Romanche transform-fault earthquake (Hicks et al. 2020), the 2018 Peru earthquake (Hu et al. 2021), and the 2020 Elazig, Turkey earthquake (Gallovič et al. 2020). With the exception of the 2011 Tohoku-Oki earthquake, where the backward rupture followed an overshooting rupture near the free surface (Ide et al. 2011), these earthquakes have in common an initial weak rupture which triggers a main rupture, at a point distant from the hypocenter,

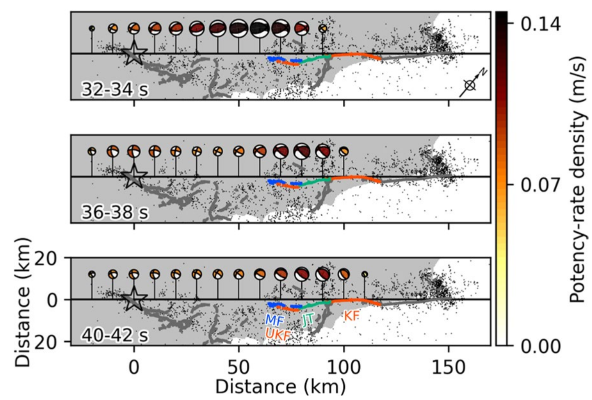

Fig. 6 Map views showing selected snapshots of potency-rate density tensors (lower-hemisphere projections) between 32 and 42 s in the top row of the entire model plane. Black dots represent aftershocks during the week after the mainshock (Lanza et al. 2019). Gray, orange, blue, and green lines indicate surface faults (Langridge et al. 2016)

that involves a back-propagating rupture. It appears that the 2016 Kaikoura earthquake is another example of this kind of event.

Our modeling approach requires few assumptions of modeling; that is, we solve for multiplicity of fault configuration and diverse rupture geometries on the flat single model fault. This is still prone to non-uniqueness in the Kaikoura rupture, primarily due to the limited spatial resolution of teleseismic records, but the rupture directions and timing, involving back-rupture propagation resolved in our model, in turn, can be useful for further inverse and/or forward modeling using near-field datasets, which contribute to converge to a realistic source model of the Kaikoura earthquake.

6 Conclusions

We revealed the source process of the 2016 Kaikoura earthquake by a potency density tensor inversion from teleseismic P-waveform data, a method for which we did not need to strictly define the fault geometry and rupture directions. We found complex episodes including an initial unilateral and a delayed main bilateral rupture, and the variations of the focal mechanisms are consistent with the reported surface ruptures. The initial rupture propagated northeastward at deep depths, when it passed through a gap in reported surface ruptures. The main rupture involved the southwestward back-rupture propagation, and it branched out and propagated into the Jordan Thrust and Papatea fault from the Kekerengu fault. Our result suggests that teleseismic waveform data can resolve such a complex rupture process, and the potency density tensor inversion approach of projecting slips on multiple faults onto a single model plane, as opposed to an approach of prescribing fault planes, is useful for analyzing earthquakes with complex fault geometries.

Abbreviations

GCMT Global Centroid Moment Tensor
PDTI Potency density tensor inversion

Supplementary Information

The online version contains supplementary material available at https://doi.org/10.1186/s40645-023-00565-z.

Additional file 1: **Tables S1 and S2.** Velocity structure models used for calculating the Green's function. **Figure S1.** Comparison of waveforms sampled at different intervals. **Figure S2.** Waveform fitting between observed and synthetic waveforms. **Figure S3.** Full snapshots of potency-rate density evolution for the obtained source model of the 2016 Kaikoura earthquake. **Figure S4.** Potency-rate density evolution along the strike direction of the model plane. **Figure S5.** Waveform fitting between input and output waveforms for the reproducibility test using the result of the analysis for real waveforms as input. **Figure S6**. Snapshots of potency-rate density evolution before 55 s for reproducibility test using waveforms generated from the obtained source model as input. **Figure S7**. Snapshots of potency-rate density evolution after 56 s for reproducibility test using waveforms generated from the obtained source model as input. **Figure S8.** Snapshots of potency-rate density evolution for sensitivity test using 1-D velocity structure near the epicenter determined based on CRUST1.0. **Figure S9.** Comparison of snapshots of potency-rate density evolution before 55 s for the preferred source model using the vertical model plane sensitivity test under the assumption of the horizontal model plane. **Figure S10.** Comparison of snapshots of potency-rate density evolution after 56 s for the preferred source model using the vertical model plane sensitivity test under the assumption of the horizontal model plane. **Figure S11.** Comparison of the obtained potency-rate density tensors during 60–66 s and visual summary of moment tensor transition between two endmembers: PF and HP-JTKF-NF.

Acknowledgements

We would like to thank Editor František Gallovič and Reviewers Thomas Ulrich and Jiří Zahradník for their thorough evaluation and constructive suggestions, which have led to significant improvements of our work. We thank Federica Lanza for providing their relocated aftershock data (Lanza et al. 2019). The facilities of IRIS Data Services, and specifically the IRIS Data Management Center, provided access to waveforms, related metadata, and derived products used in this study. IRIS Data Services are funded through the Seismological Facilities for the Advancement of Geoscience (SAGE) Award of the National Science Foundation under Cooperative Support Agreement EAR-1851048. We used FPSPACK (Gasperini and Vannucii 2003) software to handle the focal mechanism obtained in the inversion. The code for the PDTI was developed by Yuji Yagi, Kosuke Shimizu, and Shinji Yamashita. All of the figures were generated with Matplotlib (v3.4.0:https://doi.org/10.1109/MCSE.2007.55) (Hunter 2007) and Pyrocko (v2021.9.14:https://doi.org/10.5880/GFZ.2.1.2017.001) (Heimann et al. 2017).

Author contributions

KO and YY designed this study, compiled the data, and performed the analyses. All authors interpreted the research results. KO prepared figures and wrote the manuscript, which was revised by YY, SY, RO, SH, and YF. All authors approved the manuscript. All authors agreed both to be personally accountable for their own contributions and to ensure that questions related to the accuracy or integrity of any part of the work were appropriately investigated and resolved and their resolution documented in the literature.

Funding

This work was supported by Grant-in-Aid for Scientific Research (C) 22K03751 from the Ministry of Education, Culture, Sports, Science and Technology (MEXT).

Availability of data and materials

All seismic data were downloaded through the IRIS Wilber 3 system (https://ds.iris.edu/wilber3/) or IRIS Web Services (https://service.iris.edu/), including the following seismic networks: (1) BDSN (https://doi.org/10.7932/BDSN), (2) SCSN (https://doi.org/10.7914/SN/CI), (3) GEOSCOPE (https://doi.org/10.18715/GEOSCOPE.G), (4) GEOFON (https://doi.org/10.14470/TR560404), (5) the Global Telemetered Seismograph Network (https://doi.org/10.7914/SN/GT), (6) the Hong Kong Seismograph Network, (7) the New China Digital Seismograph Network (https://doi.org/10.7914/SN/IC), (8) the IRIS/IDA Seismic Network (https://doi.org/10.7914/SN/II), and (9) the Global Seismograph Network (https://doi.org/10.7914/SN/IU). The CRUST1.0 and CRUST2.0 structural velocity models are available from https://igppweb.ucsd.edu/~gabi/crust1.html and https://igppweb.ucsd.edu/~gabi/crust2.html, respectively.

Declarations

Competing interests

The authors declare no competing interests. Correspondence and requests for materials should be addressed to K.O. or Y.Y.

Received: 15 February 2023 Accepted: 23 June 2023
Published online: 10 July 2023

References

Akaike H (1980) Likelihood and the Bayes procedure. Trab Estad Investig Oper 31:143–166. https://doi.org/10.1007/BF02888350

Bai Y, Lay T, Cheung KF, Ye L (2017) Two regions of seafloor deformation generated the tsunami for the 13 November 2016, Kaikoura, New Zealand earthquake. Geophys Res Lett 44:6597–6606. https://doi.org/10.1002/2017GL073717

Bassin C, Laske G, Masters G (2000) The current limits of resolution for surface wave tomography in North America. EOS Trans AGU 81:F897

Bird P (2003) An updated digital model of plate boundaries. Geochem Geophys Geosyst. https://doi.org/10.1029/2001GC000252

Cesca S, Zhang Y, Mouslopoulou V, Wang R, Saul J, Savage M, Heimann S, Kufner SK, Oncken O, Dahm T (2017) Complex rupture process of the Mw 7.8, 2016, Kaikoura earthquake, New Zealand, and its aftershock sequence. Earth Planet Sci Lett 478:110–120. https://doi.org/10.1016/j.epsl.2017.08.024

Clark KJ, Nissen EK, Howarth JD, Hamling IJ, Mountjoy JJ, Ries WF, Jones K, Goldstien S, Cochran UA, Villamor P, Hreinsdóttir S, Litchfield NJ, Mueller C, Berryman KR, Strong DT (2017) Highly variable coastal deformation in the 2016 MW 7.8 Kaikōura earthquake reflects rupture complexity along a transpressional plate boundary. Earth Planet Sci Lett 474:334–344. https://doi.org/10.1016/j.epsl.2017.06.048

DeMets C, Gordon RG, Argus DF, Stein S (1994) Effect of recent revisions to the geomagnetic reversal time scale on estimates of current plate motions. Geophys Res Lett 21:2191–2194. https://doi.org/10.1029/94GL02118

Duputel Z, Rivera L (2017) Long-period analysis of the 2016 Kaikoura earthquake. Phys Earth Planet Inter 265:62–66. https://doi.org/10.1016/j.pepi.2017.02.004

Dziewonski AM, Chou TA, Woodhouse JH (1981) Determination of earthquake source parameters from waveform data for studies of global and regional seismicity. J Geophys Res 86:2825–2852. https://doi.org/10.1029/JB086iB04p02825

Ekström G, Nettles M, Dziewoński AM (2012) The global CMT project 2004–2010: centroid-moment tensors for 13,017 earthquakes. Phys Earth Planet Inter 200–201:1–9. https://doi.org/10.1016/j.pepi.2012.04.002

Fan W, Shearer PM (2015) Detailed rupture imaging of the 25 April 2015 Nepal earthquake using teleseismic P waves. Geophys Res Lett 42:5744–5752. https://doi.org/10.1002/2015GL064587

Frohlich C (2001) Display and quantitative assessment of distributions of earthquake focal mechanisms. Geophys J Int 144:300–308. https://doi.org/10.1046/j.1365-246x.2001.00341.x

Gallovič F, Zahradník J, Plicka V, Sokos E, Evangelidis C, Fountoulakis I, Turhan F (2020) Complex rupture dynamics on an immature fault during the 2020 Mw 6.8 Elazığ earthquake, Turkey. Commun Earth Environ. https://doi.org/10.1038/s43247-020-00038-x

Gasperini P, Vannucii G (2003) FPSPACK: a package of FORTRAN subroutines to manage earthquake focal mechanism data. Comput Geosci 29:893–901. https://doi.org/10.1016/S0098-3004(03)00096-7

Hamling IJ, Hreinsdóttir S, Clark K, Elliott J, Liang C, Fielding E, Litchfield N, Villamor P, Wallace L, Wright TJ, D'Anastasio E, Bannister S, Burbidge D, Denys P, Gentle P, Howarth J, Mueller C, Palmer N, Pearson C, Power W, Barnes P, Barrell DJA, Van Dissen R, Langridge R, Little T, Nicol A, Pettinga J, Rowland J, Stirling M (2017) Complex multifault rupture during the 2016 Mw 7.8 Kaikōura earthquake, New Zealand. Science. https://doi.org/10.1126/science.aam7194

Heimann S, Kriegerowski M, Isken M, Cesca S, Daout S, Grigoli F, Juretzek C, Megies T, Nooshiri N, Steinberg A, Sudhaus H, Vasyura-Bathke H, Willey T, Dahm T (2017) Pyrocko—an open-source seismology toolbox and library. GFZ Data Serv. https://doi.org/10.5880/GFZ.2.1.2017.001

Hicks SP, Okuwaki R, Steinberg A, Rychert CA, Harmon N, Abercrombie RE, Bogiatzis P, Schlaphorst D, Zahradnik J, Kendall JM, Yagi Y, Shimizu K, Sudhaus H (2020) Back-propagating supershear rupture in the 2016 M w 7.1 Romanche transform fault earthquake. Nat Geosci 13:647–653. https://doi.org/10.1038/s41561-020-0619-9

Holden C, Kaneko Y, D'Anastasio E, Benites R, Fry B, Hamling IJ (2017) The 2016 Kaikōura earthquake revealed by kinematic source inversion and seismic wavefield simulations: slow rupture propagation on a geometrically complex crustal fault network. Geophys Res Lett 44:11320–11328. https://doi.org/10.1002/2017GL075301

Hollingsworth J, Ye L, Avouac JP (2017) Dynamically triggered slip on a splay fault in the Mw 7.8, 2016 Kaikoura (New Zealand) earthquake. Geophys Res Lett 44:3517–3525. https://doi.org/10.1002/2016GL072228

Hu Y, Yagi Y, Okuwaki R, Shimizu K (2021) Back-propagating rupture evolution within a curved slab during the 2019 Mw 8.0 Peru intraslab earthquake. Geophys J Int 227:1602–1611. https://doi.org/10.1093/gji/ggab303

Hunter JD (2007) Matplotlib: a 2D graphics environment. Comput Sci Eng 9:90–95. https://doi.org/10.1109/MCSE.2007.55

Ide S, Baltay A, Beroza GC (2011) Shallow dynamic overshoot and energetic deep rupture in the 2011 Mw 9.0 Tohoku-Oki earthquake. Science 332:1426–1429. https://doi.org/10.1126/SCIENCE.1207020/SUPPL_FILE/1207020-IDE-SOM.PDF

Kennett BLN, Engdahl ER, Buland R (1995) Constraints on seismic velocities in the Earth from traveltimes. Geophys J Int 122:108–124. https://doi.org/10.1111/j.1365-246X.1995.tb03540.x

Kikuchi M, Kanamori H (1991) Inversion of complex body waves—III. Bull Seismol Soc Am 81:2335–2350. https://doi.org/10.1785/BSSA0810062335

Klinger Y, Okubo K, Vallage A, Champenois J, Delorme A, Rougier E, Lei Z, Knight EE, Munjiza A, Satriano C, Baize S, Langridge R, Bhat HS (2018) Earthquake damage patterns resolve complex rupture processes. Geophys Res Lett 45:10279–10287. https://doi.org/10.1029/2018GL078842

Langridge R, Ries W, Litchfield N, Villamor P, Van Dissen R, Barrell D, Rattenbury M, Heron D, Haubrock S, Townsend D, Lee J, Berryman K, Nicol A, Cox S, Stirling M (2016) The New Zealand active faults database. NZ J Geol Geophys 59:86–96. https://doi.org/10.1080/00288306.2015.1112818

Lanza F, Chamberlain CJ, Jacobs K, Warren-Smith E, Godfrey HJ, Kortink M, Thurber CH, Savage MK, Townend J, Roecker S, Eberhart-Phillips D (2019) Crustal fault connectivity of the M_w 7.8 2016 Kaikōura earthquake constrained by aftershock relocations. Geophys Res Lett 46:6487–6496. https://doi.org/10.1029/2019GL082780

Laske G, Masters G, Ma Z, Pasyanos M (2013) Update on CRUST10—A 1-degree global model of Earth's crust. Geophys Res Abstr 15:2658

Litchfield NJ, Villamor P, van Dissen RJ, Nicol A, Barnes PM, Barrell DJA, Pettinga JR, Langridge RM, Little TA, Mountjoy JJ, Ries WF, Rowland J, Fenton C, Stirling MW, Kearse J, Berryman KR, Cochran UA, Clark KJ, Hemphill-Haley M, Khajavi N, Jones KE, Archibald G, Upton P, Asher C, Benson A, Cox SC, Gasston C, Hale D, Hall B, Hatem AE, Heron DW, Howarth J, Kane TJ, Lamarche G, Lawson S, Lukovic B, McColl ST, Madugo C, Manousakis J, Noble D, Pedley K, Sauer K, Stahl T, Strong DT, Townsend DB, Toy V, Williams J, Woelz S, Zinke R (2018) Surface rupture of multiple crustal faults in the 2016 Mw 7.8 Kaikōura, New Zealand, earthquake. Bull Seismol Soc Am 108:1496–1520. https://doi.org/10.1785/0120170300

Liu J, Zahradník J (2020) The 2019 MW 5.7 Changning Earthquake, Sichuan Basin, China: a shallow doublet with different faulting styles. Geophys Res Lett. https://doi.org/10.1029/2019GL085408

Mitchell JS, Mackay KA, Neil HL, Mackay EJ, Pallentin A, Notman P (2012) Undersea New Zealand, 1:5,000,000. NIWA Chart Misc Ser 92

Mouslopoulou V, Saltogianni V, Nicol A, Oncken O, Begg J, Babeyko A, Cesca S, Moreno M (2019) Breaking a subduction-termination from top to bottom: the large 2016 Kaikōura Earthquake, New Zealand. Earth Planet Sci Lett 506:221–230. https://doi.org/10.1016/j.epsl.2018.10.020

Okuwaki R, Fan W (2022) Oblique convergence causes both thrust and strike-slip ruptures during the 2021 M 7.2 Haiti earthquake. Geophys Res Lett. https://doi.org/10.1029/2021GL096373

Okuwaki R, Hirano S, Yagi Y, Shimizu K (2020) Inchworm-like source evolution through a geometrically complex fault fueled persistent supershear rupture during the 2018 Palu Indonesia earthquake. Earth Planet Sci Lett. https://doi.org/10.1016/j.epsl.2020.116449

Okuwaki R, Hicks SP, Craig TJ, Fan W, Goes S, Wright TJ, Yagi Y (2021) Illuminating a contorted slab with a complex Intraslab rupture evolution during the 2021 Mw 7.3 East Cape, New Zealand. Earthquake. https://doi.org/10.1029/2021GL095117

Sato DSK, Fukahata Y, Nozue Y (2022) Appropriate reduction of the posterior distribution in fully Bayesian inversions. Geophys J Int. https://doi.org/10.1093/gji/ggac231

Shimizu K, Yagi Y, Okuwaki R, Fukahata Y (2020) Development of an inversion method to extract information on fault geometry from teleseismic data. Geophys J Int 220:1055–1065. https://doi.org/10.1093/gji/ggz496

Stirling MW, Litchfield NJ, Villamor P, Van Dissen RJ, Nicol A, Pettinga J, Barnes P, Langridge RM, Little T, Barrell DJA, Mountjoy J, Ries WF, Rowland J, Fenton C, Hamling I, Asher C, Barrier A, Benson A, Bischoff A, Borella J, Carne R, Cochran UA, Cockroft M, Cox SC, Duke G, Fenton F, Gasston C, Grimshaw C, Hale D, Hall B, Hao KX, Hatem A, Hemphill-Haley M, Heron DW, Howarth J, Juniper Z, Kane T, Kearse J, Khajavi N, Lamarche G, Lawson S, Lukovic B, Madugo C, Manousakis I, Mccoll S, Noble D, Pedley K, Sauer K, Stah T, Strong DT, Townsend DB, Toy V, Villeneuve M, Wandres A, Williams J, Woelz S, Zinke R (2017) THE M W 7.8 2016 Kaikōura earthquake: surface fault rupture and seismic hazard context. Bull N Z Soc Earthq Eng 50:73–84

Tadapansawut T, Okuwaki R, Yagi Y, Yamashita S (2021) Rupture process of the 2020 Caribbean Earthquake along the oriente transform fault, involving Supershear rupture and geometric complexity of fault. Geophys Res Lett. https://doi.org/10.1029/2020GL090899

Tadapansawut T, Yagi Y, Okuwaki R, Yamashita S, Shimizu K (2022) Complex rupture process on the conjugate fault system of the 2014 Mw 6.2 Thailand earthquake. Prog Earth Planet Sci. https://doi.org/10.1186/s40645-022-00484-5

Turhan F, Acarel D, Plicka V, Bohnhoff M, Polat R, Zahradník J (2023) Coseismic faulting complexity of the 2019 Mw 5.7 Silivri Earthquake in the Central Marmara seismic gap offshore Istanbul. Seismol Res Lett 94:75–86. https://doi.org/10.1785/0220220111

Ulrich T, Gabriel AA, Ampuero JP, Xu W (2019) Dynamic viability of the 2016 Mw 7.8 Kaikōura earthquake cascade on weak crustal faults. Nat Commun. https://doi.org/10.1038/s41467-019-09125-w

Wang D, Chen Y, Wang Q, Mori J (2018a) Complex rupture of the 13 November 2016 Mw 7.8 Kaikoura, New Zealand earthquake: comparison of high-frequency and low-frequency observations. Tectonophysics 733:100–107. https://doi.org/10.1016/j.tecto.2018.02.004

Wang T, Wei S, Shi X, Qiu Q, Li L, Peng D, Weldon RJ, Barbot S (2018b) The 2016 Kaikōura earthquake: simultaneous rupture of the subduction interface and overlying faults. Earth Planet Sci Lett 482:44–51. https://doi.org/10.1016/j.epsl.2017.10.056

Williams CA, Eberhart-Phillips D, Bannister S, Barker DHN, Henrys S, Reyners M, Sutherland R (2013) Revised interface geometry for the Hikurangi

subduction zone, New Zealand. Seismol Res Lett 84:1066–1073. https://doi.org/10.1785/0220130035
Xu W, Feng G, Meng L, Zhang A, Ampuero JP, Bürgmann R, Fang L (2018) Transpressional rupture cascade of the 2016 Mw 7.8 Kaikoura Earthquake, New Zealand. J Geophys Res Solid Earth 123:2396–2409. https://doi.org/10.1002/2017JB015168
Yabuki T, Matsu'ura M (1992) Geodetic data inversion using a Bayesian information criterion for spatial distribution of fault slip. Geophys J Int 109(2):363–375. https://doi.org/10.1111/j.1365-246X.1992.tb00102.x
Yagi Y, Fukahata Y (2011) Introduction of uncertainty of Green's function into waveform inversion for seismic source processes. Geophys J Int 186:711–720. https://doi.org/10.1111/j.1365-246X.2011.05043.x
Yagi Y, Okuwaki R, Enescu B, Hirano S, Yamagami Y, Endo S, Komoro T (2014) Rupture process of the 2014 Iquique Chile Earthquake in relation with the foreshock activity. Geophys Res Lett 41:4201–4206. https://doi.org/10.1002/2014GL060274
Yagi Y, Okuwaki R, Enescu B, Lu J (2023) Irregular rupture process of the 2022 Taitung, Taiwan, earthquake sequence. Sci Rep. https://doi.org/10.1038/s41598-023-27384-y
Yamashita S, Yagi Y, Okuwaki R, Shimizu K, Agata R, Fukahata Y (2021) Consecutive ruptures on a complex conjugate fault system during the 2018 Gulf of Alaska earthquake. Sci Rep 11:5979. https://doi.org/10.1038/s41598-021-85522-w
Yamashita S, Yagi Y, Okuwaki R (2022a) Irregular rupture propagation and geometric fault complexities during the 2010 Mw 7.2 El Mayor-Cucapah earthquake. Sci Rep 12:4575. https://doi.org/10.1038/s41598-022-08671-6
Yamashita S, Yagi Y, Okuwaki R, Shimizu K, Agata R, Fukahata Y (2022b) Potency density tensor inversion of complex body waveforms with time-adaptive smoothing constraint. Geophys J Int 231:91–107. https://doi.org/10.1093/gji/ggac181
Zhang H, Koper KD, Pankow K, Ge Z (2017) Imaging the 2016 Mw 7.8 Kaikoura, New Zealand, earthquake with teleseismic P waves: a cascading rupture across multiple faults. Geophys Res Lett 44:4790–4798. https://doi.org/10.1002/2017GL073461
Zheng A, Wang M, Yu X, Zhang W (2018) Source rupture process of the 2016 Kaikoura, New Zealand earthquake estimated from the kinematic waveform inversion of strong-motion data. Geophys J Int 212:1736–1746. https://doi.org/10.1093/gji/ggx505

Publisher's Note